nature COMMUNICATIONS

ARTICLE

https://doi.org/10.1038/s41467-019-09918-z OPEN

# Optimizing reaction paths for methanol synthesis from $CO_2$ hydrogenation via metal-ligand cooperativity

Yizhen Chen[1,3], Hongliang Li[1,3], Wanghui Zhao[1,3], Wenbo Zhang[1], Jiawei Li[1], Wei Li[2], Xusheng Zheng[1], Wensheng Yan[1], Wenhua Zhang[1], Junfa Zhu[1], Rui Si[2] & Jie Zeng[1]

As diversified reaction paths exist over practical catalysts towards $CO_2$ hydrogenation, it is highly desiderated to precisely control the reaction path for developing efficient catalysts. Herein, we report that the ensemble of Pt single atoms coordinated with oxygen atoms in MIL-101 ($Pt_1$@MIL) induces distinct reaction path to improve selective hydrogenation of $CO_2$ into methanol. $Pt_1$@MIL achieves the turnover frequency number of 117 $h^{-1}$ in DMF under 32 bar at 150 °C, which is 5.6 times that of $Pt_n$@MIL. Moreover, the selectivity for methanol is 90.3% over $Pt_1$@MIL, much higher than that (13.3%) over $Pt_n$@MIL with CO as the major product. According to mechanistic studies, $CO_2$ is hydrogenated into HCOO* as the intermediate for $Pt_1$@MIL, whereas COOH* serves as the intermediate for $Pt_n$@MIL. The unique reaction path over $Pt_1$@MIL not only lowers the activation energy for the enhanced catalytic activity, but also contributes to the high selectivity for methanol.

[1] Hefei National Laboratory for Physical Sciences at the Microscale, Key Laboratory of Strongly-Coupled Quantum Matter Physics of Chinese Academy of Sciences, National Synchrotron Radiation Laboratory, Key Laboratory of Surface and Interface Chemistry and Energy Catalysis of Anhui Higher Education Institutes, Department of Chemical Physics, University of Science and Technology of China, 230026 Hefei, Anhui, People's Republic of China. [2] Shanghai Synchrotron Radiation Facility, Shanghai Institute of Applied Physics, Chinese Academy of Sciences, 201204 Shanghai, People's Republic of China. [3] These authors contributed equally: Yizhen Chen, Hongliang Li, Wanghui Zhao. Correspondence and requests for materials should be addressed to R.S. (email: sirui@sinap.ac.cn) or to J.Z. (email: zengj@ustc.edu.cn)

Hydrogenation of $CO_2$ into fuels and useful chemicals serves as an important process which helps to alleviate the dearth of fossil fuels[1–17]. According to both experimental and theoretical studies, $CO_2$ hydrogenation involves various reaction paths[4–6]. Even for the first step to activate $CO_2$, $CO_2$ can be decomposed into CO*, transformed into carboxyl intermediate (COOH*), or hydrogenated into formate intermediate (HCOO*)[6–9]. Over practical catalysts, diversified reaction paths inevitably coexist, which induces the formation of different products such as CO, methane, formic acid, methanol, higher alcohols, and even gasoline, generally limiting the selectivity for the target product[10–14]. For instance, $Cu/ZnO/Al_2O_3$ catalysts have already been applied to realize gas-phase $CO_2$ hydrogenation into methanol in industry, but suffer from the limited selectivity (<70%) for methanol and stringent reaction conditions (50–100 bar, 200–300 °C)[15,16]. Catalyzed by $Cu/ZnO/Al_2O_3$, $CO_2$ undergoes reverse water-gas shift path (RWGS) to produce CO* via the formation of COOH* species[17]. Since such catalysts also involve high energy barrier for the transformation of CO*, a large proportion of CO* is directly desorbed from the catalyst surfaces to form gaseous CO, competing over further hydrogenation into methanol[17]. Recently, constructing highly active interfaces such as $Cu/CeO_x$, Cu/ZnO, and $Cu/ZrO_2$ interfaces has been reported to efficiently lower the energy barrier for the transformation of CO*, which not only increases the selectivity for methanol but also elevates the catalytic activity[18–23]. In addition, another pivotal approach is based on engineering the coordination environment of active metal atoms by alloying[24,25]. For instance, the fabrication of NiGa catalysts was found to suppress the RWGS path, thereby facilitating the production of methanol[26]. $Co_4N$ nanosheets were reconstructed into $Co_4NH_x$ during aqueous $CO_2$ hydrogenation into methanol, wherein the amido-hydrogen atoms directly added $CO_2$ to form HCOO*[4]. Despite of these achievements, it is still highly desiderated to efficiently control the reaction path for developing highly active and selective catalysts toward $CO_2$ hydrogenation.

Herein, we demonstrate that metal-ligand cooperativity in Pt single atoms encapsulated in MIL-101 ($Pt_1$@MIL) varies the reaction path and improves the selective hydrogenation of $CO_2$ into methanol relative to nanocrystal counterparts ($Pt_n$@MIL). In $Pt_1$@MIL, every Pt single atom and its coordinated O atoms compose an active center. During $CO_2$ hydrogenation, the turnover frequency (TOF) number of $Pt_1$@MIL reaches 117 $h^{-1}$ in DMF under 32 bar at 150 °C, being 5.6 times as high as that (21 $h^{-1}$) of $Pt_n$@MIL. Moreover, the selectivity for methanol reaches 90.3% over $Pt_1$@MIL, whereas the major product for $Pt_n$@MIL is CO with the selectivity of 57.5%. The cooperativity between Pt single atoms and their coordinated O atoms in $Pt_1$@MIL enables the dissociation of $H_2$ to form O–H groups. The hydroxy H atoms add into $CO_2$ to produce HCOO* as the intermediates. As for $Pt_n$@MIL, Pt–H is formed, wherein H atoms hydrogenate $CO_2$ into COOH* as the intermediates. The unique reaction path over $Pt_1$@MIL not only lowers the activation energy for the enhanced catalytic activity, but also contributes to the high selectivity for methanol.

## Results

**Synthesis and structural characterizations of $Pt_1$@MIL**. MIL-101 is a typical MOF which consists of $\mu_3$-oxo bridged Cr(III)-trimers cross linked by terephthalic acid[27,28]. The high specific surface area of $S_{Langmuir} = 5900\ m^2\ g^{-1}$ and large pore volume of ca. 2.0 $cm^3\ g^{-1}$ render MIL-101 high adsorption capacities, making it an attractive candidate for gas adsorption. As such, MIL-101 with an average particle size of 500 nm was synthesized based on previous literatures[27,28] (Supplementary Fig. 1), serving as the support in this work. In a typical synthesis of $Pt_1$@MIL, $K_2PtCl_4$ and $NaBH_4$ aqueous solutions were added into the flask containing MIL-101 aqueous solution via a syringe pump under magnetic stirring. In $Pt_1$@MIL, the Pt mass loading was determined as 0.2% by inductively coupled plasma–atomic emission spectroscopy (ICP–AES). Figure 1a shows a high-angle annular dark-field scanning transmission electron microscopy (HAADF–STEM) image of $Pt_1$@MIL. As manifested by brightness, Pt atoms were atomically dispersed in MIL-101 in the absence of nanoparticles. To highlight the dopant atoms, the magnified HAADF–STEM image and its corresponding color-coded intensity map were shown in Fig. 1b, c, indicating the isolated distribution of Pt atoms. After $Pt_1$@MIL was further washed for different rounds, the ratio of Pt to Cr remained almost unchanged, confirming that Pt single atoms were indeed anchored in MIL-101, rather than serving as a residual (Supplementary Fig. 2). By simply increasing the concentrations of $K_2PtCl_4$ and $NaBH_4$ aqueous solutions, $Pt_n$@MIL with the Pt mass loading of 1.0% was facilely synthesized. As shown in the HAADF–STEM image of $Pt_n$@MIL, Pt nanocrystals with an average size of 1.8 nm were observed (Supplementary Fig. 3). The ratio of surface Pt atoms in $Pt_n$@MIL was determined as 41.5% by CO pulse chemisorptions (Supplementary Fig. 4). To characterize the electronic properties of the obtained samples, we conducted X-ray photoelectron spectroscopy (XPS) measurements of $Pt_1$@MIL and $Pt_n$@MIL. As shown in Fig. 1d, the Pt species in $Pt_1$@MIL was determined to be at $Pt^{2+}$ state. By comparison, most of Pt species in $Pt_n$@MIL was at the metallic state, whereas a small portion of Pt was oxidized.

The X-ray absorption near-edge spectroscopy (XANES) and extended X-ray absorption fine structure (EXAFS) were measured to determine the electronic and coordination structures of Pt atoms in Pt@MIL catalysts. The Pt $L_3$-edge XANES profiles in Fig. 1e indicate that the Pt species in $Pt_1$@MIL were in a higher oxidation state than those in $Pt_n$@MIL, according to the stronger intensity for white line. It is worth noting that the spectrum of $Pt_n$@MIL was similar to that of Pt foil, indicating the metallic state of Pt species in $Pt_n$@MIL, consistent with the XPS results (Fig. 1d). As shown in EXAFS in *R* space (Fig. 1f), $Pt_1$@MIL exhibited a prominent peak at 2.01 Å from the Pt–O shell with a coordination number (*CN*) of 3.7 (Supplementary Table 1). No other typical peaks for Pt–Pt contribution at longer distances (>2.5 Å) were observed, revealing the isolated dispersion of Pt atoms throughout the whole $Pt_1$@MIL. As for $Pt_n$@MIL, a new peak at 2.76 Å was observed, corresponding to the Pt–Pt metallic bond with a *CN* of 7.4.

To investigate the location and coordination of Pt single atoms in MIL-101, density functional theory (DFT) calculations were performed to establish the atomic model of $Pt_1$@MIL. The building unit of MIL-101 comprises terephthalic linkers and an inorganic trimer. The trimer consists of three Cr atoms in an octahedral coordination. The vertices of octahedral coordination around each Cr atom are occupied by four O atoms from carboxylate groups in terephthalic linkers, one $\mu_3$O atom in the middle of Cr trimers, and one O atom from the terminal water or fluorine group. Both XPS and XANES results indicate an oxidation state assignment of $Pt^{2+}$ for $Pt_1$@MIL (Fig. 1d, e). In $Pt_1$@MIL, the individual Pt atom was stabilized by O atoms in a planar four-coordinate geometry with one O atom in carboxyl, one dangling O connected with a Cr atom, and one $O_2$ moiety (Fig. 1g and Supplementary Fig. 5). This optimized model is consistent with the oxidation state of $Pt^{2+}$ indicated by XPS and XANES results, because $Pt^{2+}$ generally adopts the $dsp^2$ hybridization which results in the planar four-coordinate geometry. To further confirm the Pt oxidation states in this model, we have compared the charge of the Pt atom in $Pt_1$@MIL with that in

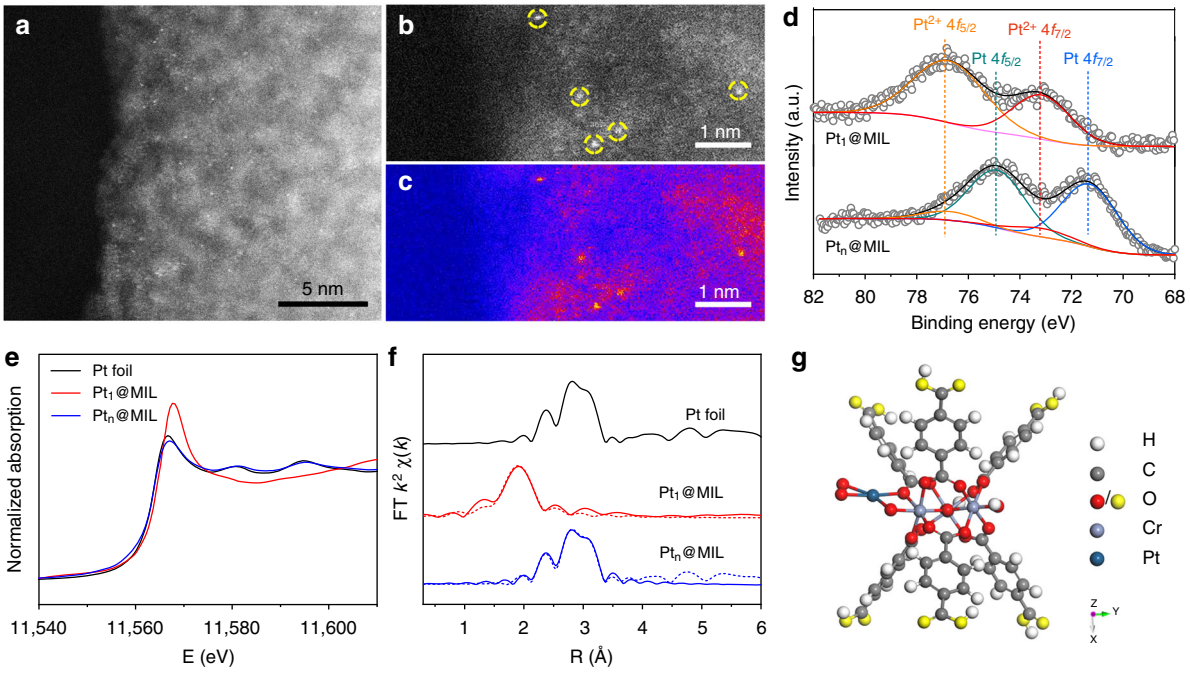


**Fig. 1** Structural characterizations of Pt@MIL. **a** HAADF-STEM image of $Pt_1$@MIL. **b**, **c** Magnified HAADF-STEM image and its corresponding color-coded intensity map of $Pt_1$@MIL. Pt single atoms marked in yellow circles were uniformly anchored in MIL-101. **d** XPS spectra of Pt 4*f* for $Pt_1$@MIL and $Pt_n$@MIL. **e** Pt $L_3$-edge XANES profiles of Pt foil, $Pt_1$@MIL, and $Pt_n$@MIL. **f** Pt $L_3$-edge EXAFS spectra in *R* space of Pt foil, $Pt_1$@MIL, and $Pt_n$@MIL. Pt foil was used as the reference. **g** Structural model of $Pt_1$@MIL simulated by DFT calculations. Blue, violet, red, gray, and white spheres represent for Pt, Cr, O, C, and H atoms, respectively. The yellow spheres represent the oxygen atoms which are fixed at their positions in crystal

isolated Pt–O and O–Pt–O clusters as representatives of $Pt^{2+}$ and $Pt^{4+}$ (Supplementary Fig. 6). Based on Mullinken analysis, the charges of Pt atoms in Pt–O and O–Pt–O clusters are +0.72 and +1.52 e, respectively. The Pt single atom in $Pt_1$@MIL is + 0.59 e charged, approximating to that in Pt–O cluster. Thus, the oxidation state of Pt in $Pt_1$@MIL was assigned to +2. Moreover, the model of the Pt single atom coordinated with four O atoms in $Pt_1$@MIL matches our EXAFS result in terms of the *CN* of Pt–O.

**Catalytic properties of $Pt_1$@MIL for $CO_2$ hydrogenation**. The catalytic properties of the as-obtained Pt@MIL in $CO_2$ hydrogenation were evaluated in a slurry reactor with 10 mL of DMF under 32 bar of $CO_2/H_2$ mixed gas ($CO_2$:$H_2$ = 1:3) at 150 °C. As a benchmark, commercial $Cu/ZnO/Al_2O_3$ (63 wt% Cu) was directly purchased from Alfa Aesar, with the ratio of surface Cu atoms to total atoms determined as 32.5% (Supplementary Fig. 7). For each catalytic test, the amounts of $Pt_1$@MIL and $Pt_n$@MIL were controlled at 500 and 240 mg, respectively, to keep the same amount (1.0 mg) of exposed Pt atoms, whereas 20 mg of $Cu/ZnO/Al_2O_3$ was used. When the reaction was catalyzed by MIL-101, the product was below detection limit (Fig. 2a). As for $Pt_1$@MIL, 0.6 mmol of products were generated after 1 h, whereas the product yield was 0.12 mmol for $Pt_n$@MIL. More importantly, the selectivity for methanol reached 90.3% over $Pt_1$@MIL with the production of formic acid as the by-product (Fig. 2a). With regard to $Pt_n$@MIL, the major product was CO with the selectivity of 57.5%, while the selectivities for formic acid, methanol, and methane were 11.1%, 13.3%, and 18.1%, respectively (Fig. 2a). In general, Pt-based heterogeneous catalysts have been reported to be selective to CO or methane during $CO_2$ hydrogenation[29,30]. In this case, $Pt_1$@MIL did not give rise to the formation of gaseous products, behaving much differently from conventional Pt-based catalysts. As for $Cu/ZnO/Al_2O_3$, 0.16 mmol of methanol, 0.026 mmol of formic acid, and 0.024 mmol of CO were formed after 1 h (Fig. 2a and Supplementary Fig. 8). To compare the catalytic activity more accurately, we calculated the TOF numbers of these catalysts by only taking Pt atoms into account based on the reaction profile at the initial stage. The TOF number of $Pt_1$@MIL reached 117 $h^{-1}$ in DMF under 32 bar at 150 °C, being around 5.6 times that (21 $h^{-1}$) of $Pt_n$@MIL and 39 times that (3 $h^{-1}$) of $Cu/ZnO/Al_2O_3$ (Fig. 2b). As a benchmark, the activity of $Cu/ZnO/Al_2O_3$ in DMF solvent was comparable with the values obtained in a fixed-bed reactor[26,31–33]. We have further applied deuterated DMF ($C_3D_7NO$) as the solvent to replace DMF in $CO_2$ hydrogenation over $Pt_1$@MIL under 32 bar at 150 °C. The TOF number of $Pt_1$@MIL reached 107 $h^{-1}$ in $C_3D_7NO$, almost equal to the corresponding values in DMF (Supplementary Fig. 9). Accordingly, the effect of proton transfer in DMF on $CO_2$ hydrogenation over $Pt_1$@MIL could be neglected.

To explore the differences in catalytic properties between $Pt_1$@MIL and $Pt_n$@MIL, we conducted a series of catalytic tests under 32 bar of $CO_2/H_2$ mixed gas ($CO_2$:$H_2$ = 1:3) at different temperatures. As shown in Fig. 2b, $Pt_1$@MIL exhibited much higher catalytic activity than $Pt_n$@MIL (Supplementary Figs. 10 and 11). Arrhenius plots were obtained based on the linear fitting of *ln*TOF vs. 1000/T (Fig. 2c). The activation energy for $Pt_1$@MIL was 76.4 kJ $mol^{-1}$, much lower than that (119.7 kJ $mol^{-1}$) for $Pt_n$@MIL. To investigate the size effect, Pt nanoparticles with an average size of 1.2 nm on MIL-101 were prepared and evaluated under 32 bar at 150 °C (Supplementary Fig. 12). The TOF number was calculated to be 22 $h^{-1}$ which was lower than that (117 $h^{-1}$) of $Pt_1$@MIL and basically the same as that (21 $h^{-1}$) of $Pt_n$@MIL with 1.8-nm Pt nanoparticles (Supplementary Fig. 13). As such, $Pt_1$@MIL exhibited higher catalytic activity and selectivity for methanol than $Pt_n$@MIL even with tiny Pt clusters.

To explore stability of $Pt_1$@MIL, we performed successive rounds of reaction. For each round, the catalytic reaction

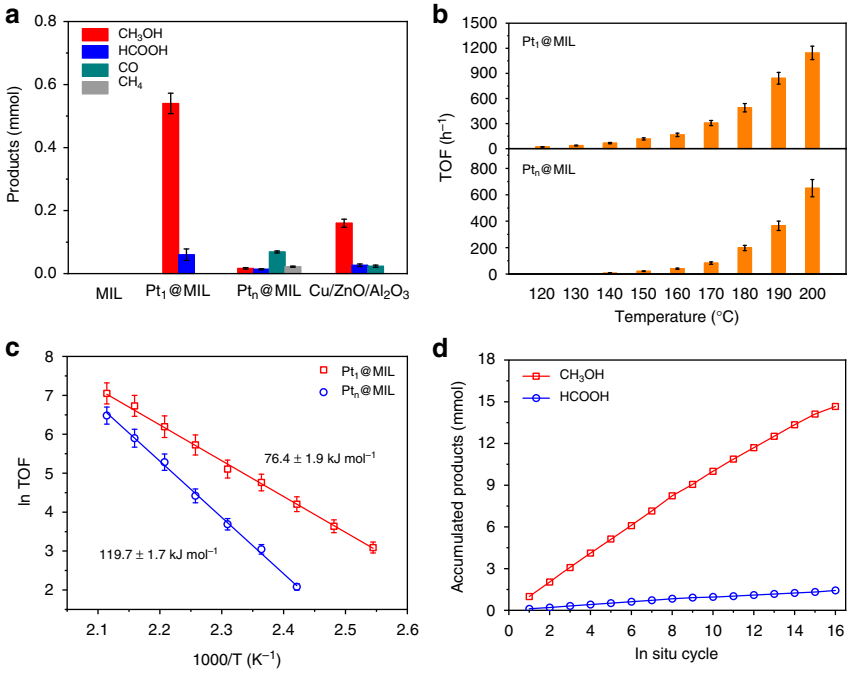


**Fig. 2** Catalytic performance of Pt@MIL in $CO_2$ hydrogenation. **a** Comparison of products obtained by using MIL-101, $Pt_1$@MIL, $Pt_n$@MIL, and commercial $Cu/ZnO/Al_2O_3$ in DMF under $CO_2/H_2$ mixed gas ($CO_2$:$H_2$ = 1:3, 32 bar) at 150 °C after 1 h. **b** Comparison of TOF numbers of $Pt_1$@MIL and $Pt_n$@MIL in DMF under $CO_2/H_2$ mixed gas ($CO_2$:$H_2$ = 1:3, 32 bar) at different temperatures. **c** The Arrhenius plots of $Pt_1$@MIL and $Pt_n$@MIL. **d** Products obtained by conducting in-situ cycles over $Pt_1$@MIL. For each cycle, the catalytic reaction proceeded under 32 bar of $CO_2/H_2$ mixed gas ($CO_2/H_2$ = 1:3) at 150 °C for 6 h. For each catalytic test, the amounts of $Pt_1$@MIL and $Pt_n$@MIL were controlled at 500 and 240 mg, respectively, to keep the same amount (1.0 mg) of exposed Pt atoms. Error bars represent standard deviation from three independent measurements

proceeded at 150 °C for 1 h. After 10 rounds, the selectivity of methanol kept almost unchanged (Supplementary Fig. 14). Moreover, the HAADF-STEM image of the used $Pt_1$@MIL ("used" refers to the catalyst after 10 rounds) showed that Pt atoms were still atomically dispersed in MIL-101 without the formation of nanoparticles (Supplementary Fig. 15). In addition, only 2.6% of Pt species in $Pt_1$@MIL was leached after 10 rounds as revealed by ICP-AES. To further investigate the potential industrial application, we tested $Pt_1$@MIL for successive in-situ cycles of reaction. For each cycle, the catalytic reaction proceeded under 32 bar of $CO_2/H_2$ mixed gas ($CO_2/H_2$ = 1:3) at 150 °C for 6 h without the removal of catalysts from the reactor during the whole test. After 16 in-situ cycles (96 h in total), $Pt_1$@MIL led to the generation of about 14.6 mmol of methanol and 1.4 mmol of formic acid in total, exhibiting high long-term stability (Fig. 2d). Accordingly, $Pt_1$@MIL was highly stable during $CO_2$ hydrogenation, thereby exhibiting potential industrial application.

**Formation of hydroxyl groups in $Pt_1$@MIL under $H_2$.** We conducted DFT calculations to investigate the hydrogen dissociation on $Pt_1$@MIL. Based on DFT calculations, the whole reaction path is divided into three elementary steps that include the dissociation of $H_2$ on Pt (step i), the formation of the first hydroxyl (step ii), and the formation of the second hydroxyl (step iii) (Supplementary Table 2 and Supplementary Fig. 16). Specially, $H_2$ is firstly dissociated on Pt to form Pt–H bonds. Afterwards, the two dissociated H atoms on Pt atoms stepwise migrates to the dangling $O_2$ moiety, resulting in the formation of two hydroxyl groups. Among these steps, step ii exhibits the highest energy barrier with the value of 0.79 eV, indicating that the formation of hydroxyl groups are able to proceed at 150 °C. To support this point, we carried out in-situ diffuse reflectance infrared Fourier transform spectroscopy (DRIFTS) measurements. Figure 3 shows the in-situ DRIFTS spectra of $Pt_1$@MIL and $Pt_n$@MIL after the treatment with $H_2$ at 150 °C for 0.5 h. As for $Pt_1$@MIL, a peak at 3197 $cm^{-1}$ appeared, corresponding to the stretching vibration of O–H. The observation of O–H and absence of Pt–H are consistent with the DFT results. With regard to $Pt_n$@MIL, the peak at 1949 $cm^{-1}$ was assigned to the stretching vibration of Pt–H. Therefore, Pt single atom activates its coordinated O atoms to adsorb the dissociated H atoms with the formation of two hydroxyl groups. As for $Pt_n$@MIL, Pt nanoparticles directly dissociate $H_2$ to form Pt–H species.

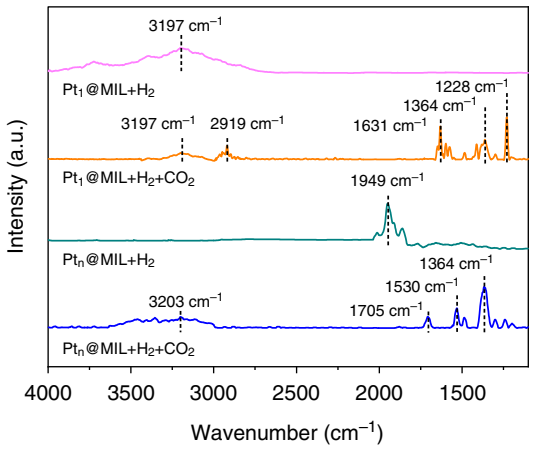


**Fig. 3** Adsorption properties of reactants on Pt@MIL. In-situ DRIFTS spectra of $Pt_1$@MIL and $Pt_n$@MIL after the treatment with $H_2$, as well as $H_2$ and $CO_2$ in sequence at 150 °C

To investigate the role played by H atoms in hydroxyl groups, we have explored the kinetic isotope effect (KIE) with the use of $D_2$ in catalytic tests. When the reaction proceeded under $CO_2/D_2$ mixed gas ($CO_2$:$D_2$ = 1:3) at 150 °C, the TOF numbers of

$Pt_1$@MIL and $Pt_n$@MIL were 21 $h^{-1}$ and 13 $h^{-1}$, respectively (Supplementary Fig. 17a–b). The KIE value refers to the ratio of the TOF using $H_2$ as the reactant gas to that using $D_2$ ($k_H/k_D$). As shown in Supplementary Fig. 17c, the KIE value of $Pt_1$@MIL was 5.6 much higher than that (1.6) of $Pt_n$@MIL. As such, the bond cleavage of O-D rather than Pt-D was involved in the reaction over $Pt_1$@MIL.

**$CO_2$ hydrogenation paths**. The different adsorption properties of H atoms on $Pt_1$@MIL and $Pt_n$@MIL induced the variation of reaction paths in $CO_2$ hydrogenation. To investigate the reaction path, we calculated the addition of the first H atom into $CO_2$. For $Pt_1$@MIL, the energy of HCOO* is 0.26 eV lower than that of COOH* (Supplementary Fig. 18a–b and Tables 3–4). In this case, the first H atom adds to the C atom in $CO_2$ to form HCOO* as the stable intermediate on $Pt_1$@MIL. In comparison, $Pt_n$@MIL favors the generation of COOH* whose energy is 0.34 eV lower than that of HCOO* (Supplementary Fig. 18c–d and Tables 3–4). As such, the transformation of $CO_2$ into COOH* serves as the dominating reaction channel on $Pt_n$@MIL. To support this point, we conducted in-situ DRIFTS measurements of $Pt_1$@MIL and $Pt_n$@MIL after the treatment with $H_2$ and $CO_2$ in sequence at 150 °C. For $Pt_1$@MIL, the peak for O–H at 3197 $cm^{-1}$ was still observed, but its intensity was weakened relative to the case when the sample was only treated with $H_2$ (Fig. 3). The peak at 1364 $cm^{-1}$ was observed, indicating the formation of $CO_2^{\delta-}$ species[4,18]. Moreover, the peaks at 2919, 1631, and 1228 $cm^{-1}$ also emerged, which were assigned to the stretching vibration of C–H, the asymmetrical and symmetrical stretching vibrations of the bidentate O–C–O in HCOO* species, respectively (Fig. 3). As for $Pt_n$@MIL treated with $H_2$ and $CO_2$ in sequence relative to the one solely exposed to $H_2$, the peak for Pt–H disappeared. Moreover, besides the peak for $CO_2^{\delta-}$, the peaks at 3203, 1705, and 1530 $cm^{-1}$ appeared, corresponding to the stretching vibration of O–H, the stretching vibration of C=O, and the bending vibration of C–O in COOH* species, respectively (Fig. 3). The in-situ DRIFTS results indicate that HCOO* and COOH* served as the intermediates for $Pt_1$@MIL and $Pt_n$@MIL, respectively, consistent with the theoretical results.

The alteration of intermediates in $CO_2$ hydrogenation over $Pt_1$@MIL and $Pt_n$@MIL was further supported by quasi-situ XPS. Quasi-situ XPS measurements were conducted after the treatment of the samples with $H_2$ and $CO_2$ in sequence at 150 °C in a reaction cell attached to the XPS end-station. As shown in Fig. 4a, the C 1*s* spectra exhibited four typical peaks at 284.6, 288.6, 289.5, and 291.0 eV, corresponding to benzene ring in MIL-101 (Ph), carboxyl group in MIL-101 (Ph-COO), HCOO*, and COOH*, respectively[18,34–36]. In addition, different species could also be distinguished in O 1*s* spectra. Specifically, the peaks at 531.5 and 532.4 eV derived from the oxygen atoms in Ph–COO and HCOO*, respectively (Fig. 4b). Two peaks at 530.0 and 531.1 eV were assigned to the carbonyl and hydroxyl species in COOH*, respectively (Fig. 4b)[34–36]. As indicated by quasi-situ XPS spectra, HCOO* or COOH* was not observed for MIL-101. Therefore, the intermediates for $Pt_1$@MIL and $Pt_n$@MIL were determined as HCOO* and COOH*, respectively, consistent with in-situ DRIFTS results.

The intrinsic difference between HCOO* and COOH* lies in the exclusive existence of C–H bond in HCOO* and O–H bond in COOH*, which could be verified by C and O K-edge XANES measurements. Figure 4c shows the C K-edge XANES profiles of $Pt_1$@MIL and $Pt_n$@MIL before/after the treatment with $H_2$ and $CO_2$ in sequence at 150 °C. Before gas treatment, both $Pt_1$@MIL and $Pt_n$@MIL revealed the same XANES profiles which exhibited seven characteristic features. In detail, three features at 285.0, 285.9, and 290.3 eV were assigned to the excitations of the C=C π antibonding orbital for benzene ring in MIL-101 ($\pi^*$(Ph))[37]. Besides, the peaks at 287.6, 288.5, 289.4, and 293.1 eV corresponded to the excitations of the C–H antibonding orbital ($\sigma^*$(C–H)), the C = O π antibonding orbital ($\pi^*$(C=O)), the C–O antibonding orbital ($\sigma^*$(C–O)), and the σ antibonding orbital for

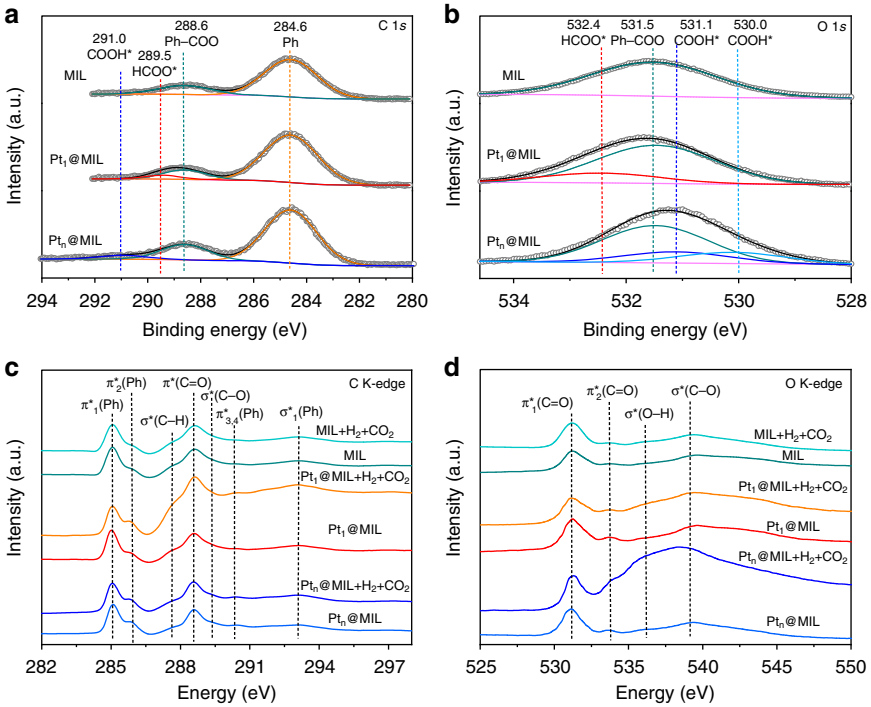


**Fig. 4** Mechanistic insight into remarkable activity of $Pt_1$@MIL. **a**, **b** Quasi-situ XPS spectra of C 1*s* and O 1*s* for MIL-101, $Pt_1$@MIL, and $Pt_n$@MIL after the treatment with $H_2$ and $CO_2$ in sequence at 150 °C, respectively. **c**, **d** C and O K-edge XANES spectra for MIL-101, $Pt_1$@MIL, and $Pt_n$@MIL before/after the treatment with $H_2$ and $CO_2$ in sequence at 150 °C, respectively

benzene ring in MIL-101 ($\sigma^*$(Ph)), respectively[37]. After the treatment of MIL-101 with $H_2$ and $CO_2$ in sequence at 150 °C, the features were almost the same as the corresponding ones before the treatment. After the sequential gas treatment, the profiles of $Pt_1$@MIL and $Pt_n$@MIL both showed stronger feature of $\pi^*$(C=O) relative to that without gas treatment, indicating the transformation of $CO_2$. Moreover, the feature of $\sigma^*$(C–H) became stronger for $Pt_1$@MIL, but remained almost unchanged for $Pt_n$@MIL. As such, only the species generated over $Pt_1$@MIL contained C–H bond. As for O K-edge XANES, the features at 531.1 and 533.7 eV corresponded to the excitations of the $\pi^*$(C=O), while the features at 536.1 and 539.1 eV were assigned to the O–H antibonding orbital ($\sigma^*$(O–H)) and the C–O antibonding orbital ($\sigma^*$(C–O)), respectively[38] (Fig. 4d). After the exposure to $H_2$ and $CO_2$ in sequence at 150 °C, the feature of $\sigma^*$(O–H) became significantly stronger for $Pt_n$@MIL, but stayed almost the same for $Pt_1$@MIL. Accordingly, only $Pt_n$@MIL induced the generation of species containing O–H groups.

In $Pt_1$@MIL, every Pt single atom and its coordinated O atoms composed an active center. The metal-ligand cooperativity leads to the dissociation of $H_2$ to form hydroxyl groups, wherein hydroxy H atoms added into $CO_2$ to produce HCOO* as the intermediates. With regards to $Pt_n$@MIL, Pt hydrides formed, offering H atoms to hydrogenate $CO_2$ into COOH* as the intermediates. In general, HCOO* is reported to be hydrogenated into HCOOH* and finally converted into methanol[6,9]. By comparison, besides forming HCOOH*, COOH* is also apt to lose the hydroxyl species to generate CO* species[6,18]. CO* can be either directly desorbed to form gaseous CO, or further hydrogenated into methane[6]. Thus, experiencing the reaction path via COOH* intermediate over $Pt_n$@MIL leads to the formation of gaseous products.

## Discussion

In conclusion, the metal-ligand cooperativity in $Pt_1$@MIL was found to induce distinct reaction path and improve selective hydrogenation of $CO_2$ into methanol relative to $Pt_n$@MIL. According to mechanistic studies, $CO_2$ was hydrogenated into HCOO* as the intermediate for $Pt_1$@MIL, whereas COOH* served as the intermediate for $Pt_n$@MIL. The unique reaction path over $Pt_1$@MIL both lowered the activation energy for the enhanced activity and led to the high selectivity for methanol. Upgrading the catalysts from nanocrystals to single atoms not only enhances the atomic utilization efficiency, but also alters the catalytic mechanisms such as the adsorption of reactants or intermediates on catalysts and the reaction path. This strategy offers a powerful means to improve the catalytic performance for $CO_2$ hydrogenation, and extends our understanding of single-atom catalysis.

## Methods

**Synthesis of MIL-101**. The synthesis of MIL-101 followed a reported method[28]. Specifically, 2 g of $Cr(NO_3)_3{\cdot}9H_2O$, 830 mg of terephthalic acid, and 0.225 mL of HF aqueous solution (40.0% in mass fraction) were added into 25 mL of water in a 50-mL beaker, followed by stirring at room temperature for 15 min. Then, the solution was transferred into a 50-mL Teflon-lined autoclave and heated at 220 °C for 8 h. After the solution was cooled to room temperature, the product was collected by centrifugation, washed three times with water. For further purification, the solid product was sequentially stirred in 200 mL of ethanol solution (95% ethanol with 5% $H_2O$) at 80 °C for 24 h, 300 mL of $NH_4F$ aqueous solution (30 mM) at 70 °C for 24 h, and 200 mL of water at 90 °C for 3 h. The product was collected by centrifugation, and then dried at 60 °C under vacuum.

**Synthesis of Pt@MIL**. In a typical synthesis of $Pt_1$@MIL, 100 mg of MIL-101 were dispersed in 60 mL of water in a 250-mL flask under magnetic stirring for 10 min. 10.1 mL of $K_2PtCl_4$ aqueous solution (0.1 mM) and 10.1 mL of $NaBH_4$ aqueous solution (0.1 mM) were added into the flask through a two-channel syringe pump at a rate of 2 mL $h^{-1}$ under magnetic stirring at room temperature. The sample was washed three times with water, and dried at 60 °C under vacuum. Further ICP result determined that the mass loading of Pt was 0.2%. The synthetic procedure for $Pt_n$@MIL with the Pt loadings of 1.0% was similar to that for $Pt_1$@MIL, except for increasing the amounts of $K_2PtCl_4$ and $NaBH_4$. For $Pt_n$@MIL, 10.4 mL of $K_2PtCl_4$ aqueous solution (0.5 mM) and 10.4 mL of $NaBH_4$ aqueous solution (0.5 mM) were added into the flask through a two-channel syringe pump at a rate of 10 mL $h^{-1}$ under magnetic stirring at room temperature. The synthesis of Pt nanoparticles with an average size of 1.2 nm was similar to that of $Pt_n$@MIL except for the concentration of precursors. Specially, 100 mg of MIL-101 were dispersed in 60 mL of water in a 250-mL flask under magnetic stirring for 10 min. 10.4 mL of $K_2PtCl_4$ aqueous solution (0.3 mM) and 10.1 mL of $NaBH_4$ aqueous solution (0.5 mM) were added into the flask through a two-channel syringe pump at a rate of 10 mL $h^{-1}$ under magnetic stirring at room temperature.

**XAFS measurements**. The XAFS measurements were carried out at Pt $L_3$-edge (11564 eV) on the BL14W1 beamline[39] of Shanghai Synchrotron Radiation Facility. The XAFS data of Pt@MIL were recorded in fluorescence mode by using a Ge solid-state detector. The calibration of the energy was based on the absorption edge of pure Pt foil. The data extraction and fitting were carried out by using Athena and Artemis codes. As for XANES, the normalized absorption refers to the experimental absorption coefficients vs. energies $\mu(E)$ after background subtraction and normalization procedures. As for EXAFS, the first-shell approximation was adopted to analyze the Fourier transformed data in $R$ space of the Pt–O shell, while metallic Pt model was used to analyze that of the Pt–Pt shell. To determine the passive electron factors ($S_0^2$), the experimental Pt foil data were fitted while the $CN$ of Pt–Pt was fixed as 12. Afterwards, $S_0^2$ was fixed for further analysis. The parameters such as bond distance ($R$), $CN$, and Debye Waller ($D.W.$) factor around the absorbed atoms were variable during the fitting process.

**DFT calculations**. Density functional theory (DFT) calculations were performed using Gaussian program[40] to explain the interaction mechanism between $CO_2$ and $Pt_1$@MIL, a cluster with 30 O atoms, 48 C atoms, 3 Cr atoms, 32 H atoms, and 1 Pt atom was adopted to simulate $Pt_1$@MIL. The six carboxylate terminals on the top of benzene ring were saturated by hydrogen atoms ($COO^- \rightarrow COOH$) and the twelve oxygen atoms were fixed at their crystal positions during geometric optimization. We made calculations with B3LYP-D3 functional[41] implemented in Gaussian with the combination of the Grimme's third generation dispersion correction (D3)[42]. For structural optimization, the standard Gaussian-type basis sets 6–31 G(d)[43] was used for C, O, and H atoms and LANL2DZ[44] sets for metal atoms. As for the calculation of reaction paths, we used the optimized structure for a higher-precision single-point energy calculation. In the level, the basis sets for describing C, O, and H atoms was replaced by 6–311++G(d, p)[45], whereas the basis sets for metal atoms still adopted LANL2DZ. In order to simulate the periodic Pt (111), we used Vienna ab initio simulation package (VASP)[46,47]. The projector augmented wave (PAW) method was used to describe the interaction between ions and electrons[48]. The nonlocal exchange correlation energy was evaluated using the Perdew–Burke–Ernzerhof functional[49]. A plane wave basis set with a cutoff energy of 400 eV and a $1 \times 1 \times 1$ $k$-point grid generated by the Monkhorst–Pack method were used to describe the Brillouin zone for geometric optimization. The atomic structures were relaxed using either the conjugate gradient algorithm or the quasi-Newton scheme as implemented in the VASP code until the forces on all unconstrained atoms were ≤0.02 eV $Å^{-1}$.

**Catalytic tests of Pt@MIL catalysts in $CO_2$ hydrogenation**. The hydrogenation of $CO_2$ was conducted in a 100-mL slurry reactor (Parr Instrument Company). In a typical catalytic test, the reactor was charged and discharged with 32 bar of mixed gas ($CO_2$:$H_2$ = 1:3) at room temperature for three times, after the addition of 10 mL of DMF and certain amounts of catalysts into the Teflon inlet. For a catalytic test, the weights of $Pt_1$@MIL and $Pt_n$@MIL were controlled at 500 and 240 mg, respectively, so as to keep the same amount (1.0 mg) of exposed Pt in each catalyst. The reaction proceeded under stirring with a rate of 300 rpm and 32 bar of mixed gas ($CO_2$:$H_2$ = 1:3) at 150 °C. After the completion of the reaction, the gaseous products were determined by GC-FID and GC-TCD. The reaction mixture in liquid phase was collected by centrifugation at 11,180 × $g$ for 2 min. The test solution contained 50 μL of chloroform, as an internal standard, and 1 mL of the reaction mixture. 100 μL of the test solution was dissolved in 0.4 mL of DMSO-$d_6$ for the measurements of $^1$H NMR. For each data point, the catalytic tests were repeated thrice. For the stability of $Pt_1$@MIL, we applied two methods including successive reaction rounds and in-situ cycles. The addition of catalysts, solution, and reaction gases followed the same procedure as a typical catalytic test. Successive reaction rounds were carried out with the collection of catalysts for each round. Specially, after the proceeding of reaction at 150 °C for 1 h, both gaseous and liquid products were detected. Meanwhile, the catalysts were collected via centrifugation and washed thrice with DMF, followed by being re-added to the slurry reactor for the next round. In-situ cycles were carried out without opening the slurry reactor to collect the catalysts. For each cycle, after the proceeding of reaction at 150 °C for 6 h, both gaseous and liquid products were taken through

tubes for detection. The TOF was calculated based on the equations.

$$\mathrm{TOF} = n_{CO2}/(t \times n_{\text{surface Pt atoms}}) = n_{CO2} \times \mu_{Pt}/(t \times m_{\text{surface Pt atoms}}) \quad (1)$$

$$m_{\text{surface Pt}} = m_{cat} \times w \times r_{\text{surface}} \quad (2)$$

In this equation, $n_{CO2}$ represents the mole of converted $CO_2$ molecules. $t$ is the reaction time. $n_{\text{surface Pt atoms}}$ represents the mole of surface Pt atoms. $\mu_{Pt}$ is the weight of one mole of Pt atoms. $m_{\text{surface}}$ is the weight of surface Pt species in the catalysts. $m_{cat}$ is the weight of catalysts. $w$ represents the mass loading of Pt species. $r_{\text{surface}}$ represents the ratio of surface Pt atoms to total Pt atoms. For $Pt_1$@MIL, we assumed that all the Pt atoms were exposed on the surface, so that $r_{\text{surface}}$ is 100.0%. For $Pt_n$@MIL, $r_{\text{surface}}$ was determined as 41.5% via CO pulse chemisorptions

**In-situ DRIFTS tests**. The instrument for in-situ DRIFTS experiments was composed of an elevated-pressure cell (DiffusIR Accessory PN 041-10XX) and a Fourier transform infrared spectrometer (TENSOR II Sample Compartment RT-DLaTGS). The resolution of wavenumber was 4 $cm^{-1}$ at 150 °C. The background spectrum was obtained after a $N_2$ flow (1 bar) for 0.5 h at 150 °C. Then, 1 bar of $H_2$ was allowed to flow into the cell at the rate of 30 sccm at 150 °C for 0.5 h, followed by flowing with 1 bar of $N_2$ at the rate of 30 sccm at 150 °C for 0.5 h. To detect the species generated after the treatment of the samples with $H_2$ and $CO_2$ in sequence, 1 bar of $H_2$ was allowed to flow into the cell at the rate of 30 sccm at 150 °C for 0.5 h, followed by flowing with 1 bar of $N_2$ at the rate of 30 sccm at 150 °C for 0.5 h. Then, 1 bar of $CO_2$ was allowed to flow into the cell at 25 °C for 30 min, followed by purging with 1 bar of $N_2$ at 25 °C for 30 min.

**Quasi-situ XPS measurements**. Quasi-situ XPS measurements were performed at the photoemission end-station on the BL10B beamline of National Synchrotron Radiation Laboratory (NSRL, China). The samples were exposed to 1 bar of $H_2$ and $CO_2$ in sequence at 150 °C for 0.5 h. Afterwards, the samples were moved to the analysis chamber for further XPS analysis.

**Instrumentations**. TEM, HAADF–STEM, and STEM–EDX images were collected on a JEOL ARM-200F field-emission transmission electron microscope operating at 200 kV accelerating voltage. ICP-AES (Atomscan Advantage, Thermo Jarrell Ash, USA) was used to determine the concentration of metal species. NMR spectra were recorded on a Brucker-400 MHz spectrometer. The C and O K-edge X-ray absorption spectra were measured at beamline B12b of National Synchrotron Radiation Laboratory (NSRL, China) in the total electron yield (TEY) mode by collecting the sample drain current under a vacuum better than $1 \times 10^{-7}$ Pa.

## Data availability

The data that support the plots within this paper and other findings of this study are available from the corresponding author upon reasonable request.

Received: 11 July 2018 Accepted: 3 April 2019
Published online: 23 April 2019

## References

1. Gao, P. et al. Direct conversion of CO2 into liquid fuels with high selectivity over a bifunctional catalyst. *Nat. Chem.* **9**, 1019–1024 (2017).
2. Vogt, C. et al. Unravelling structure sensitivity in CO2 hydrogenation over nickel. *Nat. Catal.* **1**, 127–134 (2018).
3. Liu, Q. et al. Direct catalytic hydrogenation of CO2 to formate over a Schiff-base-mediated gold nanocatalyst. *Nat. Commun.* **8**, 1407 (2017).
4. Wang, L. et al. Incorporating nitrogen atoms into cobalt nanosheets as a strategy to boost catalytic activity toward CO2 hydrogenation. *Nat. Energy* **2**, 869–876 (2017).
5. Kar, S., Sen, R., Goeppert, A. & Prakash, G. K. S. Integrative CO2 capture and hydrogenation to methanol with reusable catalyst and amine: toward a carbon neutral methanol economy. *J. Am. Chem. Soc.* **140**, 1580–1583 (2018).
6. Li, Y., Chan, S. H. & Sun, Q. Heterogeneous catalytic conversion of CO2: A comprehensive theoretical review. *Nanoscale* **7**, 8663–8683 (2015).
7. Peng, Y. et al. Molecular-level insight into how hydroxyl groups boost catalytic activity in CO2 hydrogenation into methanol. *Chem* **4**, 613–625 (2018).
8. Gao, G., Jiao, Y., Waclawik, E. & Du, A. Single atom (Pd/Pt) supported on graphitic carbon nitride as an efficient photocatalyst for visible-light reduction of carbon dioxide. *J. Am. Chem. Soc.* **138**, 6292–6297 (2016).
9. Kattel, S. et al. Active sites for CO2 hydrogenation to methanol on Cu/ZnO catalysts. *Science* **355**, 1296–1299 (2017).
10. Li, H. et al. Synergetic interaction between neighbouring platinum monomers in CO2 hydrogenation. *Nat. Nanotechnol.* **13**, 411–417 (2018).
11. Nielsen, D. U., Hu, X.-M., Daasbjerg, K. & Skrydstrup, T. Chemically and electrochemically catalysed conversion of CO2 to CO with follow-up utilization to value-added chemicals. *Nat. Catal.* **1**, 244–254 (2018).
12. Zhang, X. et al. Product selectivity in plasmonic photocatalysis for carbon dioxide hydrogenation. *Nat. Commun.* **8**, 14542 (2017).
13. Nie, L. et al. Activation of surface lattice oxygen in single-atom Pt/CeO2 for low-temperature CO oxidation. *Science* **358**, 1419–1423 (2017).
14. Wei, J. et al. Directly converting CO2 into a gasoline fuel. *Nat. Commun.* **8**, 15174 (2017).
15. Spencer, M. S. The role of zinc oxide in Cu/ZnO catalysts for methanol synthesis and the water-gas shift reaction. *Top. Catal.* **8**, 259–266 (1999).
16. Kuld, S. et al. Quantifying the promotion of Cu catalysts by ZnO for methanol synthesis. *Science* **352**, 969–974 (2016).
17. Behrens, M. et al. The active site of methanol synthesis over Cu/ZnO/Al2O3 industrial catalysts. *Science* **336**, 893–897 (2012).
18. Graciani, J. et al. Highly active copper-ceria and copper-ceria-titania catalysts for methanol synthesis from CO2. *Science* **345**, 546–550 (2014).
19. Liu, C. et al. Carbon dioxide conversion to methanol over size-selected Cu4 clusters at low pressures. *J. Am. Chem. Soc.* **137**, 8676–8679 (2015).
20. Liao, F. et al. Electronic modulation of a copper/zinc oxide catalyst by a heterojunction for selective hydrogenation of carbon dioxide to methanol. *Angew. Chem. Int. Ed.* **51**, 5832–5836 (2012).
21. Wang, J. et al. A highly selective and stable ZnO-ZrO2 solid solution catalyst for CO2 hydrogenation to methanol. *Sci. Adv.* **3**, e1701290 (2017).
22. Li, C. S. et al. High-performance hybrid oxide catalyst of manganese and cobalt for low-pressure methanol synthesis. *Nat. Commun.* **6**, 6538 (2015).
23. Matsubu, J. C. et al. Adsorbate-mediated strong metal-support interactions in oxide-supported Rh catalysts. *Nat. Chem.* **9**, 120–127 (2017).
24. Khan, M. U. et al. Pt3Co octapods as superior catalysts of CO2 hydrogenation. *Angew. Chem. Int. Ed.* **55**, 9548–9552 (2016).
25. Van den Berg, R. et al. Structure sensitivity of Cu and CuZn catalysts relevant to industrial methanol synthesis. *Nat. Commun.* **7**, 13057 (2016).
26. Studt, F. et al. Discovery of a Ni-Ga catalyst for carbon dioxide reduction to methanol. *Nat. Chem.* **6**, 320–324 (2014).
27. Liu, X. H., Ma, J. G., Niu, Z., Yang, G. M. & Cheng, P. An efficient nanoscale heterogeneous catalyst for the capture and conversion of carbon dioxide at ambient pressure. *Angew. Chem. Int. Ed.* **54**, 988–991 (2015).
28. Férey, G. et al. A chromium terephthalate-based solid with unusually large pore volumes and surface area. *Science* **309**, 2040–2042 (2005).
29. Kattel, S., Yan, B. H., Chen, J. G. G. & Liu, P. CO2 hydrogenation on Pt, Pt/SiO2 and Pt/TiO2: importance of synergy between Pt and oxide support. *J. Catal.* **343**, 115–126 (2016).
30. Beaumont, S. K., Alayoglu, S., Specht, C., Kruse, N. & Somorjai, G. A. A nanoscale demonstration of hydrogen atom spillover and surface diffusion across silica using the kinetics of CO2 methanation catalyzed on spatially separate Pt and Co nanoparticles. *Nano Lett.* **14**, 4792–4796 (2014).
31. An, B. et al. Confinement of Ultrasmall Cu/ZnOx nanoparticles in metal–Organic frameworks for selective methanol synthesis from catalytic hydrogenation of CO2. *J. Am. Chem. Soc.* **139**, 3834–3840 (2017).
32. Rungtaweevoranit, B. et al. Copper nanocrystals encapsulated in Zr-based metal–organic frameworks for highly selective CO2 hydrogenation to methanol. *Nano Lett.* **16**, 7645–7649 (2016).
33. Sun, Q. et al. A novel process for the preparation of Cu/ZnO and Cu/ZnO/Al2O3 ultrafine catalyst: structure, surface properties, and activity for methanol synthesis from CO2 + H2. *J. Catal.* **167**, 92–105 (1997).
34. Mudiyanselage, K. et al. Importance of the metal-oxide interface in catalysis: In situ studies of the water-gas shift reaction by ambient-pressure X-ray photoelectron spectroscopy. *Angew. Chem. Int. Ed.* **52**, 5101–5105 (2013).
35. Prosvirin, I. P., Bukhtiyarov, A. V., Bluhm, H. & Bukhtiyarov, V. I. Application of near ambient pressure gas-phase X-ray photoelectron spectroscopy to the investigation of catalytic properties of copper in methanol oxidation. *Appl. Surf. Sci.* **363**, 303–309 (2016).
36. Deng, X. et al. Surface chemistry of Cu in the presence of CO2 and H2O. *Langmuir* **24**, 9474–9478 (2008).
37. Stöhr, J. *NEXAFS Spectroscopy* (Springer, Berlin, 1992).
38. Gordon, M. L. et al. Inner-shell excitation spectroscopy of the peptide bond: comparison of the C 1s, N 1s, and O 1s spectra of glycine, glycyl-glycine, and glycyl-glycyl-glycine. *J. Phys. Chem. A* **107**, 6144–6159 (2003).
39. Yu, H. S. et al. The XAFS beamline of SSRF. *Nucl. Sci. Tech.* **26**, 050102 (2015).
40. Frisch, M. J. et al. *Gaussian 09, Revision D.01*. (Gaussian, Inc., Wallingford CT, 2013).
41. Jiao, Y. et al. Electrocatalytically switchable CO2 capture: first principle computational exploration of carbon nanotubes with pyridinic nitrogen. *ChemSusChem* **7**, 435–441 (2014).
42. Becke, A. Density-functional thermochemistry. III. The role of exact exchange. *J. Chem. Phys.* **98**, 5648–5652 (1993).

43. Grimme, S., Antony, J., Ehrlich, S. & Krieg, H. A consistent and accurate ab initio parametrization of density functional dispersion correction (DFT-D) for the 94 elements H-Pu. *J. Chem. Phys.* **132**, 154104 (2010).
44. Hehre, W. J., Ditchfield, R. & Pople, J. A. Self-consistent molecular orbital methods. XII. Further extensions of Gaussian-type basis sets for use in molecular orbital studies of organic molecules. *J. Chem. Phys.* **56**, 2257–2261 (1972).
45. Chiodo, S., Russo, N. & Sicilia, E. LANL2DZ basis sets recontracted in the framework of density functional theory. *J. Chem. Phys.* **125**, 104107 (2006).
46. Clark, T., Chandrasekhar, J., Spitznagel, G. W. & Schleyer, P. V. R. Efficient diffuse function-augmented basis sets for anion calculations. III. The 3-21 + G basis set for first-row elements. *Li–F. J. Comp. Chem.* **4**, 294–301 (1983).
47. Kresse, G. & Furthmüller, J. Efficient iterative schemes for Ab Initio total-energy calculations using a plane-wave basis set. *Phys. Rev. B* **54**, 11169–11186 (1996).
48. Blöchl, P. E. Projector augmented-wave method. *Phys. Rev. B* **50**, 17953–17979 (1994).
49. Perdew, J. P., Burke, K. & Ernzerhof, M. Generalized gradient approximation made simple. *Phys. Rev. Lett.* **77**, 3865–3868 (1996).

## Acknowledgements

This work was supported by NSFC (21573206), Key Research Program of Frontier Sciences of the CAS (QYZDB-SSW-SLH017), Anhui Provincial Key Scientific and Technological Project (1704a0902013), Major Program of Development Foundation of Hefei Center for Physical Science and Technology (2017FXZY002), National Key Research and Development Program (2018YFA0208600), and Fundamental Research Funds for the Central Universities. This work was partially carried out at the USTC Center for Micro and Nanoscale Research and Fabrication. The calculations were performed on the supercomputing system in USTC-SCC and Guangzhou-SCC.

## Author contributions

Y.C., H.L., and Wa.Z. equally contributed to this work. Y.C., H.L., and J.Ze. designed the studies and wrote the paper. Y.C., H.L., and Wenb.Z. synthesized catalysts. Y.C., H.L., and J.L. performed catalytic tests. Wa.Z. and Wenh.Z. performed DFT calculations. Y.C., X.Z., and J.Zh. conducted XPS measurements. W.L. and R.S. conducted XAFS measurements. H.L. and W.Y. conducted XANES measurements. All authors discussed the results and commented on the manuscript.

## Additional information

**Supplementary Information** accompanies this paper at https://doi.org/10.1038/s41467-019-09918-z.

**Competing interests:** The authors declare no competing interests.

**Reprints and permission** information is available online at http://npg.nature.com/reprintsandpermissions/

**Journal peer review information:** *Nature Communications* thanks the anonymous reviewers for their contribution to the peer review of this work.

**Publisher's note:** Springer Nature remains neutral with regard to jurisdictional claims in published maps and institutional affiliations.